Enhanced strength-ductility synergy via novel bifunctional nano-precipitates in a high-entropy alloy

Liyuan Liu[a], Yang Zhang[a], Junpeng Li[a], Mingyu Fan[a], Xiyu Wang[a], Guangchuan Wu[a], Zhongbo Yang[b], Junhua Luan[c], Zengbao Jiao[d], Chain Tsuan Liu[c], Peter K Liaw[e], Zhongwu Zhang[a]

a Key Laboratory of Superlight Materials and Surface Technology, Ministry of Education, College of Materials Science and Chemical Engineering, Harbin Engineering University, Harbin 150001, China
b National Key Laboratory for Nuclear Fuel and Materials, Nuclear Power Institute of China, Chengdu 610041, China
c Department of Materials Science and Engineering, City University of Hong Kong, Hong Kong, China
d Department of Mechanical Engineering, The Hong Kong Polytechnic University, Hong Kong, China
e Department of Materials Science and Engineering, The University of Tennessee, Knoxville, TN 37996-2100, United States

Abstract

High-entropy alloys (HEAs) with a single-phased face-centered-cubic structure possess excellent plasticity but generally low strength. Precipitation strengthening is one of the most promising methods to improve the strength of alloys. However, plagued by a nerve-wracking fact that strength-ductility trade-off frequently limits the improvement of alloy properties. To overcome this problem, a new Ni35(CoFe)55V5Nb5 HEA with an excellent strength and ductility synergy was developed by introducing a novel bifunctional L12-Ni3Nb nano-precipitate. This HEA exhibits a high yield strength of 855 MPa, ultimate tensile strength of 1,302 MPa and marvelous elongation of ~ 50%. First-principles calculations show that the (Ni24Co18Fe6)3(Nb10V4Fe2) nano-precipitate with a L12 structure possesses lower formation energy than that with D022 structure. The novel nano-precipitates provide two-fold functions. On the one hand, L12-(Ni24Co18Fe6)3(Nb10V4Fe2) nano-precipitates have a high anti-phase boundary energy, contributing to a significant increment in the yield strength through precipitation strengthening. More importantly, the precipitation of the precipitates lowers the stacking fault energy (SFE) of the alloy matrix, contributing to the excellent work-hardening ability and large plasticity through activating the continuous formation of SF networks and Lomer-Cottrell locks during deformation. The strategy to introduce the novel bifunctional nano-precipitates paves a new way to enhance the strength-ductility synergy of alloys.

Keywords: High-entropy alloys; Precipitation strengthening; Nano-precipitates; Stacking fault; Mechanical properties.

1. Introduction

High-entropy alloys (HEAs), as a new class of structural materials, have attracted extensive attentions in recent years (Ding et al., 2019; Zhang et al., 2020; Pan et al., 2021; Song et al., 2020; George et al., 2019; Liu et al., 2021). In principle, HEAs possess simple random solid solutions rather than ordered and/or intermetallic phases partly due to a high entropy of mixing (Cantor et al., 2004; Yeh et al., 2004). Body-centered-cubic (BCC) HEAs possess high strength, and the refractory BCC HEAs usually exhibit excellent properties at high temperatures. However, the plasticity of HEAs with BCC structure is low (Feng et al., 2021, 2017a). Hexagonal-close-packed (HCP) HEAs are mainly highlighted in their functionality (Yuan et al., 2017). The most widely studied HEAs are face-centered-cubic (FCC) structure, which generally possess good plasticity but low strength (Li et al., 2021, 2019). If their comprehensive mechanics is optimized, they can be potential candidates for many structural applications. The deformation mechanisms and exceptional strain hardening behavior of FCC HEAs have been well revealed through different methods (Wu et al., 2018; Maity et al., 2018; Kaushik et al., 2021; Fu et al., 2021; Wang et al., 2021). To date, different strengthening mechanisms, such as phase transformation strengthening (Li et al., 2016), solid-solution strengthening (He et al., 2016; Khater et al., 2014), dislocation strengthening (Kaushik et al., 2021), grain refinement strengthening (Feng et al., 2017b; Hao et al., 2021; Baig et al., 2021) and precipitation strengthening (Ding et al., 2018; Zhao, 2020; Abdolranim et al., 2012), have also been applied to achieve high strength in FCC HEAs.

For most metals, there is usually a strength-ductility trade-off effect (Ritchie, 2011). Increasing the strength will inevitably lead to the loss of ductility, which is obviously undesirable. To overcome this, recently, numerus strategies have been tried to achieve an excellent strength-ductility synergy in HEAs. For example, the gradient nanoscaled dislocation cell structures are introduced into the FCC HEAs, improving the strength without obvious loss of ductility (Pan et al., 2021). The stacking faults (SF)-induced plasticity, the refined structures and accumulated dislocations are designed to enhance plasticity and strength (Pan et al., 2021). It is also reported that the ultrafine-grained duplex microstructures obtained by thermo-mechanical processing can also realize the excellent strength-ductility combination of HEAs, which is attributed to the two-hierarchical constraint effect and a self-generated microcrack-arresting mechanism (Shi et al., 2019). The simultaneous improvement of strength and ductility can be achieved in a gradient structure with a thin deformed layer and an undeformed core

(Hasan et al., 2019). It is interesting to note that, transformation induced plasticity (TRIP) and twinning induced plasticity (TWIP) can also occur by adjusting the composition of HEAs (Bahramyan et al., 2020; Li et al., 2016). These methods are helpful to improve the properties of the HEAs. However, different from the above methods, in this work, a new bifunctional nano-precipitate is developed to realize the strength-ductility synergy in HEAs.

Precipitation strengthening seems to be one of the most potential method to enhance the strength of HEAs. The precipitates can act as an obstacle on the dislocation slip path to hinder the dislocation slip to provide high hardening (Zhao et al., 2022). Therefore, traditional $L1_2$-$Ni_3(Al,Ti)$ and $D0_{22}$-Ni_3Nb nano-precipitates, which are widely applied in superalloys, have been successfully introduced into HEAs to improve the mechanical properties (Du et al., 2020; He et al., 2019). Although the strengthening effect of $D0_{22}$ precipitates is better than that of $L1_2$ precipitates due to its higher lattice mismatch and anti-phase boundary energy, the negative effects on plasticity is more severe (He et al., 2019). The effect of $L1_2$ precipitates is milder in strengthening, but in general, it benefits to keep a desired plasticity due to its coherent relationship with the FCC matrix (He et al., 2016). To improve the strength by $L1_2$ precipitates, the volume fraction needs to be high, but this feature will also lead to a negative effect. For instance, increasing the concentration of constituent elements in $L1_2$ precipitates may increase the risk of forming brittle intermetallic compounds or cause other processing problems (Yang et al., 2018). In addition, the size of $L1_2$ or $D0_{22}$ precipitates is usually relatively large (tens to hundreds of nanometers), which also worsens the plasticity (Zhao et al., 2022).

In general, it is difficult for large-size precipitates to overcome the strength-ductility trade-off (Philippe et al., 2013). The existence of precipitates leads to the dislocation accumulations, which improves the strength but reduces the plasticity. Many of the plastic-deformation mechanisms of crystalline alloys depend on the stacking fault energy (SFE), including dislocation slip, TWIP, and TRIP (Otto et al., 2013; Koizumi et al., 2013; Pandey et al., 2015; Pan et al., 2021; Zhang et al., 2021). This provides an opportunity to control the deformation mechanisms by composition design for tuning the SFE of alloys (Bahramyan et al., 2020). For the FCC-structural alloys with low SFE, the deformation mechanism is more inclined to form SF, twinning and even phase transformation. Oppositely, micro-banding and dislocation slip are more likely to take place under the condition of high SFE (Fan et al., 2020). It is difficult to simultaneously achieve large plasticity by the reduction of SFE and high

strength dislocation pinning. The addition of more low SFE-forming elements leads to the lower probability of dislocation slip, resulting in large plasticity but low strength (Wei et al., 2019; Kivy et al., 2017; Zhang et al., 2017). Our strategy is to reduce the SFE to enhance plasticity, while the strengthening effects are remained in HEAs.

The aim of this work is to develop a HEA with synergistic improvement of strength and ductility. Elements, Ni, Fe, and Co, are widely used as the main constituent elements in most FCC HEAs to obtain an excellent performance, specifically ductility. In Ni-containing HEAs, elements, Nb and V, can be introduced to form precipitates due to the negative mixing enthalpy ($\Delta H_{Ni-Nb} = -30$ kJ/mol, and $\Delta H_{Ni-V} = -18$ kJ/mol) (Takeuchi et al., 2005). The Ni-rich environment increases the driving force for the precipitation of the precipitates (Jiao et al., 2015). Fe and Co can enter the precipitates (an $L1_2$ phase) in a small amount, which is helpful to the inherent ductility of the precipitates (Yang et al., 2018). In addition, a small amount of V can reduce the SFE energy (Tabachnikova et al., 2017). Co is also an important element to reduce the SFE of alloys (Fan et al., 2020). Therefore, in the present work, a non-equiatomic $Ni_{35}(CoFe)_{55}V_5Nb_5$ HEA is designed. Novel bifunctional $L1_2$-Ni_3Nb nano-precipitates with small diameter (~ 5 nm) are dispersed in FCC HEA matrix through proper thermomechanical processing. Meanwhile, the SFE of the matrix is lowered through the formation of $L1_2$ nano-precipitates, inducing the continuous formation of SF networks and Lomer-Cottrell (LC) locks during deformation. Hence, the newly-developed HEA possess the large plasticity and excellent work-hardening ability by the combination of the precipitation-strengthening and the formation of SF networks.

2. Material and methods

The alloys with the nominal composition of $Ni_{35}(CoFe)_{55}V_5Nb_5$ (at.%) were developed. The alloy ingots were prepared in a vacuum-arc-melting furnace with the argon protection. The purities of all the raw materials are more than 99.9% (weight percent, wt.%). The alloys were melted five times to ensure chemical uniformity, and then drop-casted into rods of 20 mm in diameter in a water-cooled copper mold. The ingot was homogenized at 1,200 °C for 2 h and then water quenched. The homogenized ingot was cold rolled to 2.0 mm (thickness reduced by 90%), then solid-solution treated at 1,200 °C for 4 min., water quenched, and finally cold rolled again to 1.8 mm (labeled as SS). The solid-solution-treated samples (SS specimens) were then aged at 650 °C for 30 min. to obtain aged samples (labeled AG).

Tensile tests along the rolling direction were conducted, using an Instron 5566 testing machine at a strain rate of 10^{-3} s^{-1}. Three samples were tested under each condition to assure the repeatability. The gage length, width, and thickness of tensile specimens are 12.5 mm, 3.7 mm and 1.3 mm, respectively. The surfaces of test samples were polished using a 2000-grit SiC paper to eliminate scratches. A contacting Instron extensometer was used to measure the strain within the sample gage upon loading. The yield strength was determined, using the 0.2% offset plastic strain method.

The X-ray diffraction (XRD), electron backscattering diffraction (EBSD), and transmission electron microscopy (TEM) were performed to characterize the phase components and microstructures. The XRD with Cu-Kα radiation employing a D/max-2550 X-ray diffractometer was used to identify the phase components. The θ−2θ scanning was conducted in the range of 20–100° with a scanning speed of 5°/min. The EBSD measurements were carried out, using a Hitachi S3400 scanning electron microscope (SEM) equipped with an HKL Channel 5 software (Xu et al., 2019). EBSD specimens were mechanically polished and then ion-beam polished. TEM (FEI Talos F200) was employed to identify the crystal structures of the matrix and precipitates. TEM specimens were mechanically thinned to ~40 μm, punched to Φ3 mm circle sheets, and then thinned by ion-beam milling. The fracture micromorphology of the specimens after the tensile tests were characterized by SEM.

Nanoscale precipitates were characterized, using atom probe tomography (APT). The needle-shaped specimens were fabricated by lift-outs and annularly milled in an FEI Scios focused ion beam/scanning electron microscope (FIB/SEM). The APT characterizations were performed in a local electrode atom probe (CAMECA LEAP 5000 XR). The specimens were analyzed at 70 K in a voltage mode, at a pulse repetition rate of 200 kHz, a pulse fraction of 20%, and an evaporation detection rate of 0.1% atom per pulse. An Imago Visualization and Analysis Software (IVAS) version 3.8 (Han et al., 2018) was employed for creating the 3-dimension (3D) reconstructions and data analysis.

The atomic occupation and formation energy of the multicomponent nano-precipitates for both $L1_2$ and $D0_{22}$ structures were investigated by the first-principles calculations, using the density functional theory (DFT) with the CASTEP (Cambridge Sequential Total Energy Package) module of Materials Studio 8.0 package. The Perdew-Burke-Ernzerhof (PBE) parameterization of the generalized gradient approximation (GGA) was employed (Yang et al., 2018). In order to make the formation energy comparable, periodic 64-atom $2 \times 2 \times 4$ and $2 \times 2 \times 2$ supercells for $L1_2$ and $D0_{22}$ structures were

constructed to determine the total energies for each cell, respectively, corresponding to a plane-wave cutoff energy of 320 eV and 4 × 4 × 2 MonkhorstePack *k*-point meshes (Yang et al., 2018).

3. Results

3.1. Mechanical properties

Representative tensile engineering stress-strain curves and fracture morphologies of SS and AG samples are shown in **Fig. 1.** The yield strength, ultimate tensile strength, and elongation-to-fracture of SS are 334 MPa, 746 MPa, and ∼ 67%, respectively. Upon aging, the yield strength of AG is significantly increased to 855 MPa. A significant increment in yield strength (∼ 521 MPa) is obtained by nano-precipitates strengthening. Meanwhile, the ultimate tensile strength reaches as high as 1,302 MPa along with an excellent elongation of ∼ 50%, possessing a strong work-hardening capacity of 447 MPa. The fracture morphologies of both SS and AG exhibit fine-scale dimples, indicating a typical ductile fracture mechanism.
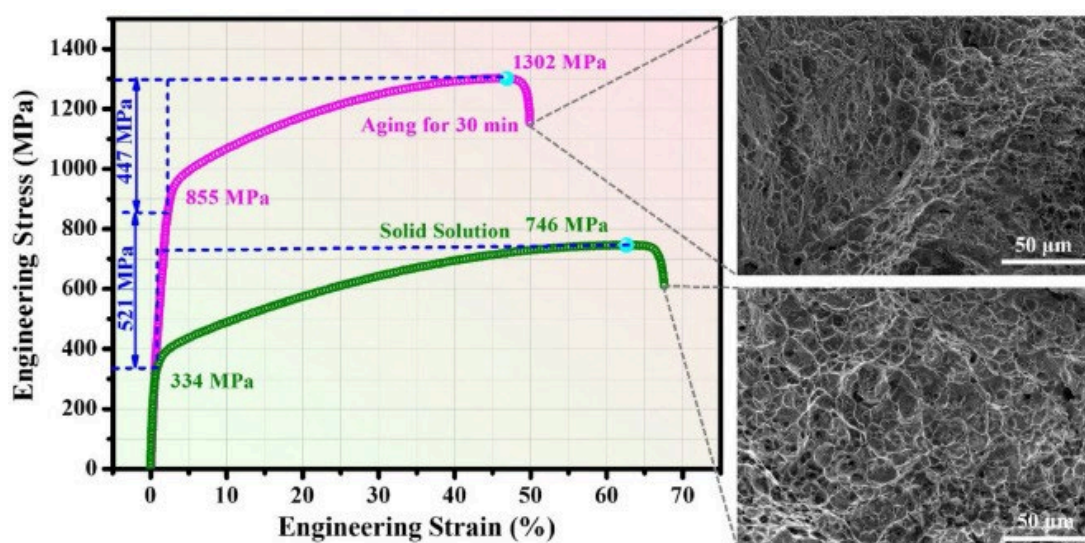

Fig. 1. Mechanical properties and fracture morphologies. Representative tensile engineering stress-strain curves of SS and AG samples at room temperature, and the corresponding fracture morphologies.

3.2. Phase composition and microstructure

The X-ray diffraction (XRD) patterns of SS and AG samples are shown in **Fig. 2**a. Both SS and AG samples have a single-phase FCC structure, and no other phases were found. The lattice parameters were determined as 0.3604 nm for SS and 0.3603 nm for AG. The electron backscattered diffraction (EBSD) images show the microstructures of SS and AG samples in **Figs. 2**b-c, respectively. Both samples exhibit a typical single-phase

composed of recrystallized equiaxed grains. The statistical distributions of grain sizes are presented in **Figs. 2**d-e, respectively. The average grain sizes of SS and AG are ~ 59 μm and ~ 61 μm, respectively. There is no obvious change of grain sizes before and after aging.
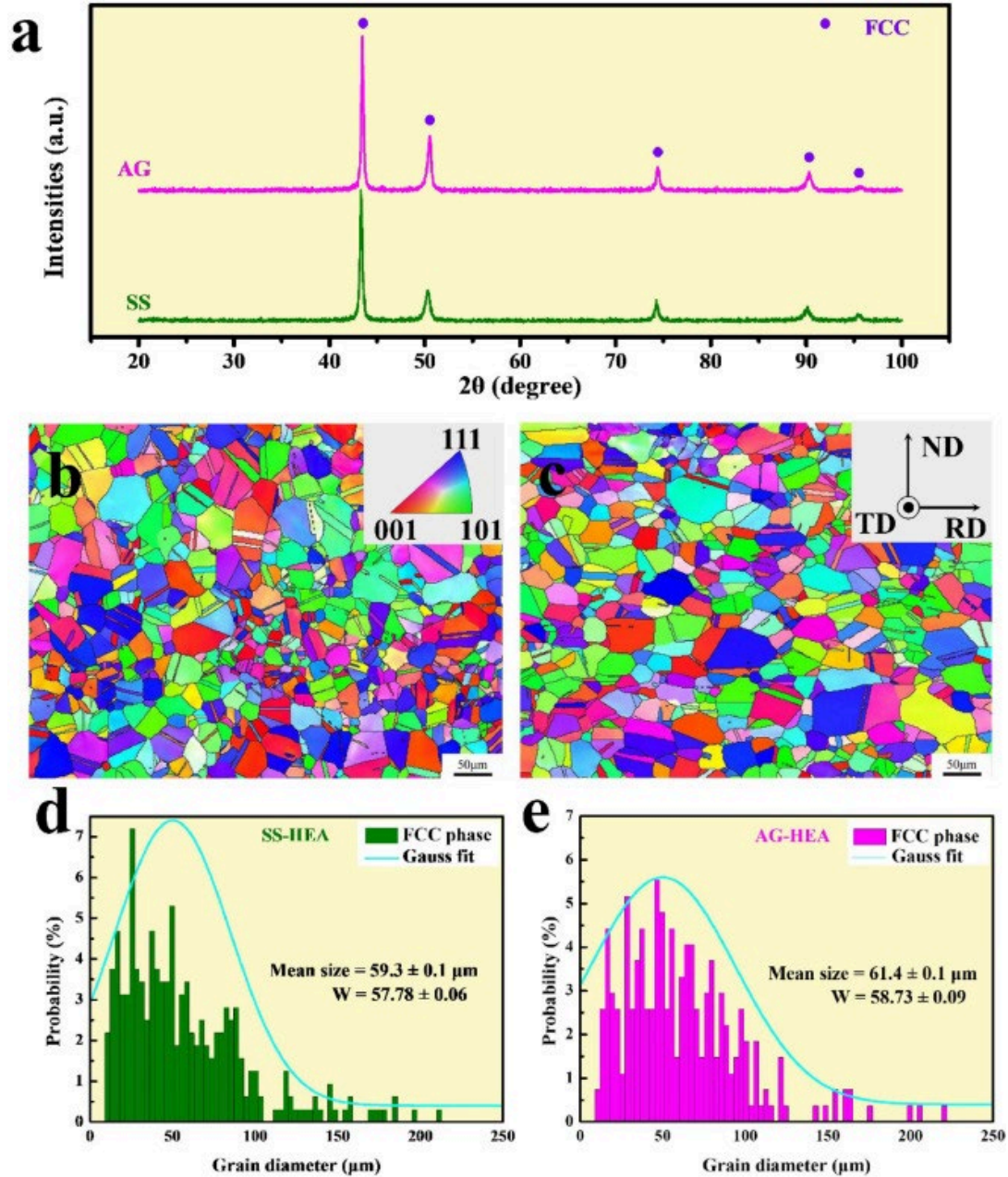

Fig. 2. Phase composition and microstructure of SS and AG. (a) XRD patterns of SS and AG samples. (b) and (c) EBSD images of SS and AG samples, respectively. (d) and (e) Grain-size distributions of SS and AG samples, respectively.

3.3. Structures and compositions of nano-precipitates

In order to explore the mechanism for the excellent mechanical properties of AG, TEM and APT were used to characterize the atomic-scale microstructure of the AG sample in detail. The bright (BF) and dark field (DF) images in the same selected area are exhibited in **Figs. 3**a-b. The DF images indicate that the approximate spherical nano-precipitates distribute uniformly in the matrix with a volume fraction of ~ 22%. **Fig. 3**c presents the diffraction pattern (DP) images along three different zone axes ([001], [011] and [112]). Two sets of diffraction patterns, corresponding to the matrix and precipitates, respectively, are observed. The main bright spots belong to the matrix, which confirms that the matrix is indeed an FCC structure. The weak spots show a typical $L1_2$ structure. The coherent FCC / $L1_2$ interface with continuous lattices is characterized by high-resolution TEM (HRTEM), as exhibited in **Fig. 3**d. **Fig. 3**e shows the relevant Fast Fourier Transform (FFT) patterns, and **Fig. 3**f exhibits the interface relationship between the precipitates and matrix. The diffraction-intensity distribution of the atomic layers through the two regions (the precipitate and matrix) along the purple arrow in **Fig. 3**b shows that the two atomic layers with lighter and heavier elements are alternately arranged in the precipitate region, while the intensity is uniform in the matrix region, as shown in **Fig. 3**g. The lattice of an ordered $L1_2$ phase is very close to that of the FCC phase. The lattice mismatch between the two phases can be described as $\delta = 2(\alpha_{L1_2}-\alpha_{matrix})/(\alpha_{matrix}+\alpha_{L1_2})$, and determined to be ~ 0.2% from the HRTEM results. Where δ is the lattice mismatch between the two phases, and α refers to the lattice parameter of each phase. The chemical concentrations of Ni, Co, Fe, Nb, and V in the precipitates and matrix were analyzed by APT, as demonstrated in **Fig. 4**a. One can observe that the $L1_2$ phase is enriched in Ni, Co, and Nb and depleted in Fe. A 10 atomic percent (at.%) Nb isoconcentration surface is used to visualize the interface between FCC and $L1_2$ phases, demonstrating the size, shape, and distribution of the nano-precipitates. The diameters of these precipitates in the APT reconstruction are ~ 5 nm. The elemental partitioning in a proximity histogram across the interface between the matrix and precipitates is shown in **Fig. 4**b. The composition of the FCC phase is 33.9Ni-27.1Co-31.2Fe-4.9V-2.9Nb (at.%), while that of the $L1_2$ phase is 38.2Ni-28.2Co-11.1Fe-6.6V-15.9Nb (at.%). The volume fraction of precipitates can be expressed by the lever rule as follows:(1)$V_{f,L12}=\dfrac{C_o-C_{matrix}}{C_{L12}-C_{matrix}}$where C_o is the nominal composition of the alloy, C_{L12} and C_{matrix} are the components of the $L1_2$ and FCC phases, respectively. As shown in **Fig. 4**c, the volume fraction of $L1_2$ phases is estimated to be

~ 18%, which is comparable with the value, 22% from TEM-DF images. According to the structure information (from TEM) and composition (from APT) of the nano-precipitates, it is interesting that the nanoscale precipitates in this newly-developed HEA possess a L1$_2$-crystal structure with the stoichiometry of (Ni, Co, Fe)$_3$(Nb, V).
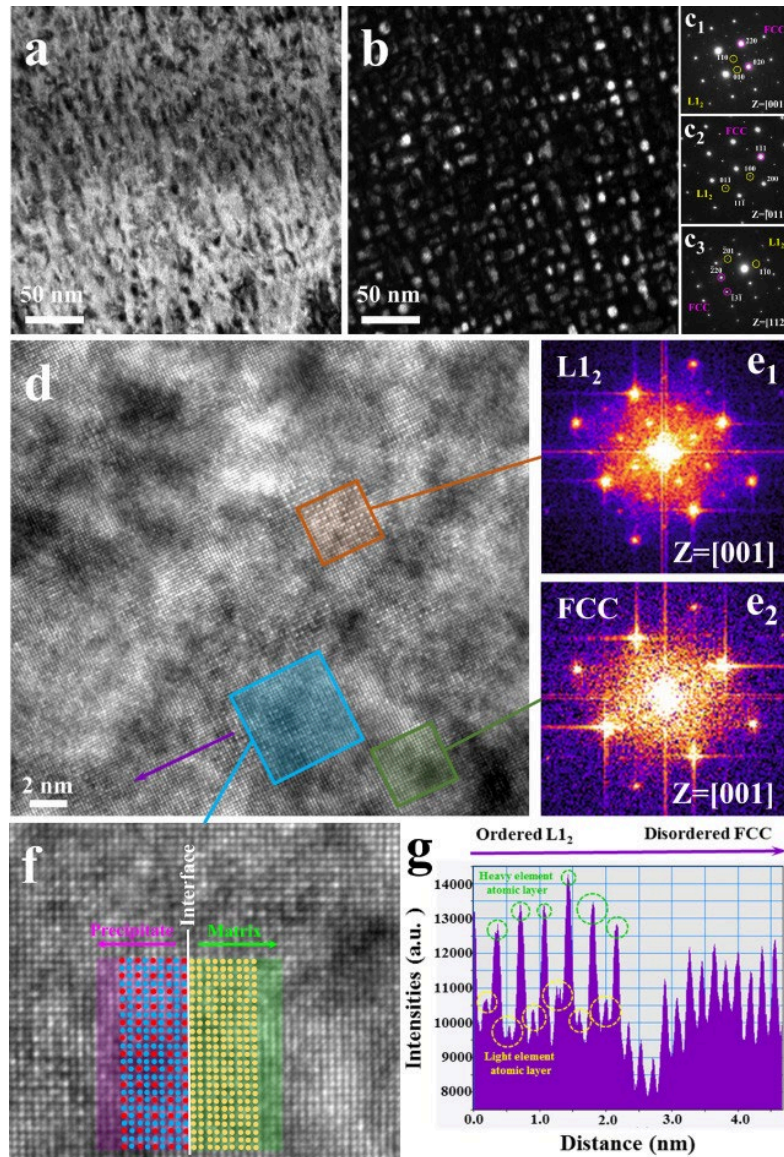

Fig. 3. Structures of nano-precipitates. (a) Bright-field and (b) Dark-field images showing that the nano-precipitates are uniformly precipitated in the matrix. (c) DP images along [001], [011] and [112] zone axes proving that the nano-precipitates have an L1$_2$ structure. (d) HRTEM image showing the precipitates and matrix. (e) FFT patterns confirming the crystal structures of the precipitates and matrix in (d). (f) Atomic-arrangement diagram showing the interface relationship between the precipitates and matrix. (g) Intensity profile as marked along the purple arrow in (d) presenting the arrangement of atomic layers in the two phases.
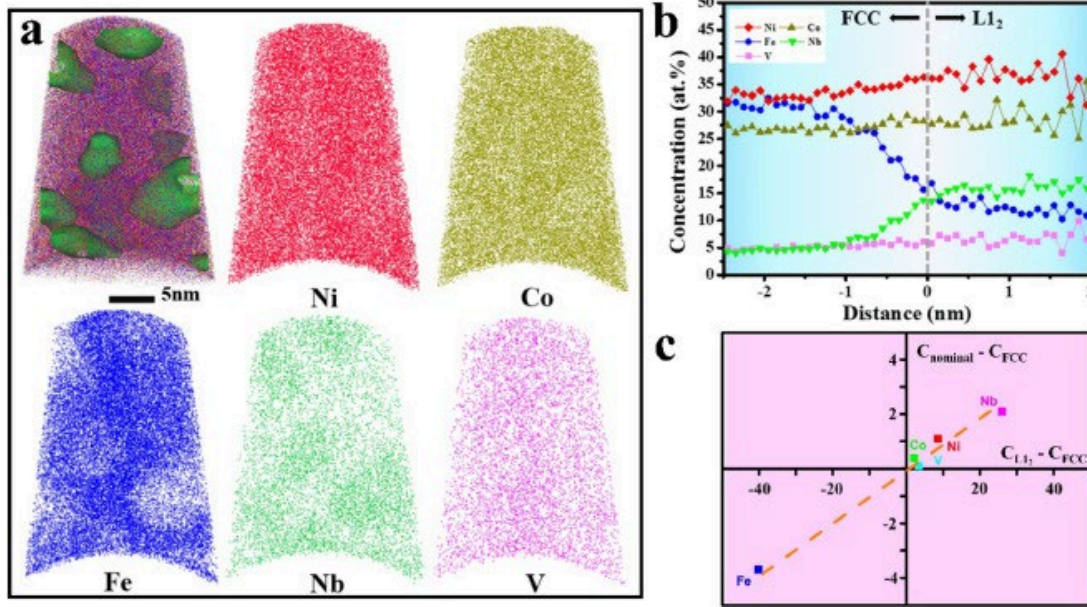
Fig. 4. Morphologies, compositions, and volume fractions of nano-precipitates. (a) APT maps with Ni, Co, Fe, Nb, and V, and isoconcentration interface plotted at 10 at.% Nb. (b) Composition distributions across the surface of the matrix and L1$_2$ phases. (c) Lever-rule diagram of the content of elements from (b), indicating the volume fraction through the slope of the line.

The structure of the nano-precipitate in AG-HEA belongs to L1$_2$-Ni$_3$Nb. The Nb and V atoms occupy the B site of an L1$_2$ phase in the A$_3$B-crystal structure. The Ni atoms occupy the A site (Fan et al., 2020), while Fe and Co atoms may occupy both A and B sites, depending on the chemical composition (Yang et al., 2018). The sum of Nb and V atoms is only $\sim$ 23 at.% from the APT results but not 25 at.%, indicating that 2 at.% of Fe or Co atoms may enter the B sublattice, as presented in **Fig. 4**b.

Here, first-principles calculations were performed, based on the APT compositional analysis in 64-atom supercells (24 Ni, 18 Co, 8 Fe, 10 Nb, and 4 V atoms). Two L1$_2$-ordered models were constructed, based on the (Ni$_{24}$Co$_{16}$Fe$_8$)(Nb$_{10}$V$_4$Co$_2$) composition with 2 at.% Co occupying the B sublattice, and the (Ni$_{24}$Co$_{18}$Fe$_6$)(Nb$_{10}$V$_4$Fe$_2$) composition with 2 at.% Fe occupying the B sublattice. The formation energy per atom in the L1$_2$-ordered models can be given by (Farkoosh et al., 2020; Scott et al., 2015):(2)$E_f = (E_{tot} - 24\mu Ni - 18\mu Co - 8\mu Fe - 10\mu Nb - 4\mu V)/64$ where E_{tot} is the total energy of a $2 \times 2 \times 4$ L1$_2$-Ni$_3$Nb supercell with 2 at.% Co and 2 at.% Fe occupying the B sublattice. μNi, μCo, μFe, μNb, and μV are the chemical potentials of pure Ni, Co, Fe, Nb, and V calculated by assuming the same cell symmetry, respectively. The results show that the formation energy of the model with Co (Model 1) or Fe (Model 2) at the B site are very close as shown in **Fig. 5**, indicating that both Fe and Co may occupy the

B site. However, Fe at the B site takes a lower formation energy, and thus, Fe occupying the B sublattice is applied in the following discussion. Therefore, the composition of L1$_2$-type precipitates in this study is determined to be $(Ni_{37.5}Co_{28.1}Fe_{9.4})(Nb_{15.6}V_{6.3}Fe_{3.1})$. A D0$_{22}$-ordered model (Model 3) was also constructed, based on the $(Ni_{24}Co_{18}Fe_6)(Nb_{10}V_4Fe_2)$ composition with 2 at.% Fe occupying the B sublattice. The results suggest that the formation energy of the D0$_{22}$ model with Fe at the B site is -1.745 eV·atom^{-1}, which is far higher than that of the L1$_2$ model (Model 2), as exhibited in **Fig. 5**, indicating that the precipitates with a L1$_2$ structure is more stable and easier to form. Therefore, it is reasonable that the precipitates in the AG-HEA system possess a L1$_2$-Ni$_3$Nb structure.
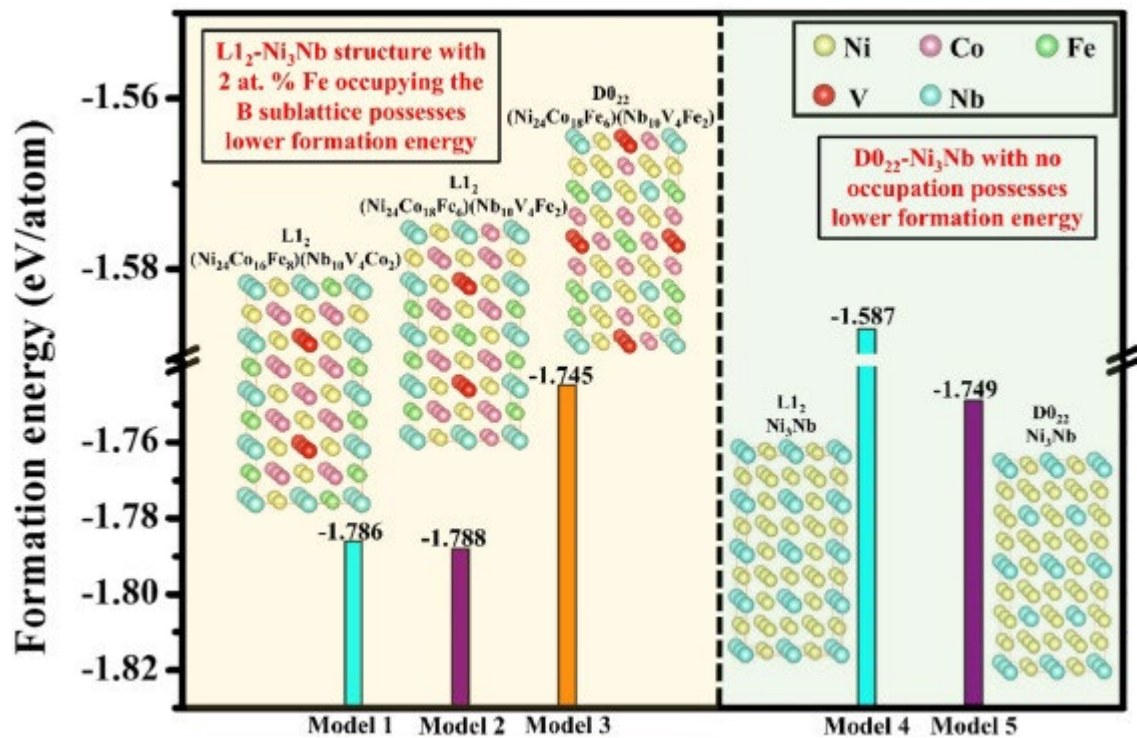

Fig. 5. Formation energy of L1$_2$- and D0$_{22}$-Ni$_3$Nb structures with various compositions. Models 1–3 show the formation energies of A$_3$B-type L1$_2$ and D0$_{22}$ structures with 2 at.% Fe or Co occupying the B sublattice. Models 4 and 5 present the effect of the crystal structures (L1$_2$ and D0$_{22}$) on the formation energy of Ni$_3$Nb.

3.4. Microstructure changes upon stress loading

In order to explore the large plasticity of AG-HEA, the microstructures of AG and SS before and after tensile fracture were characterized by TEM, as shown in **Fig. 6**. For SS and AG before tensile tests, there are only entangled dislocation configuration caused by annealing, and no other obvious structural defects caused by deformation were found (**Figs. 6**a-b). However, there are a large number of planar-slip dislocations in SS

after the tensile test (**Fig. 6**c). For AG, high-density SFs appeared after the tensile test, as exhibited in **Fig. 6**d. Both the DF and DP confirm that there are SFs, as shown in **Figs. 6**e-f, indicating that the perfect dislocation dissociates into partial dislocations and SF bands, i.e., extended dislocations (Fan et al., 2020). BF images in **Fig. 6**g shows the SFs of AG at different observation angles after the tensile test. Two {111} slip systems (yellow and red arrows marked in **Figs. 6**d and g) are activated to form a high-density and staggered SFs, constituting a wide SF networks, as shown in **Fig. 6**h. The LC locks are formed at the intersection of the SF networks, as presented in the red circle in BF of **Fig. 6**i. HRTEM shows the intersecting SF networks (white dotted lines) and LC locks (red dots) on the {111} slip system (**Fig. 6**j). The corresponding FFT image of the blue frame in **Fig. 6**j also shows the existence of intersecting SFs (**Fig. 6**k). **Fig. 6**l presents an enlarged view of a representative SF, indicating that the SF is a sequence stacked by BCABABCA.
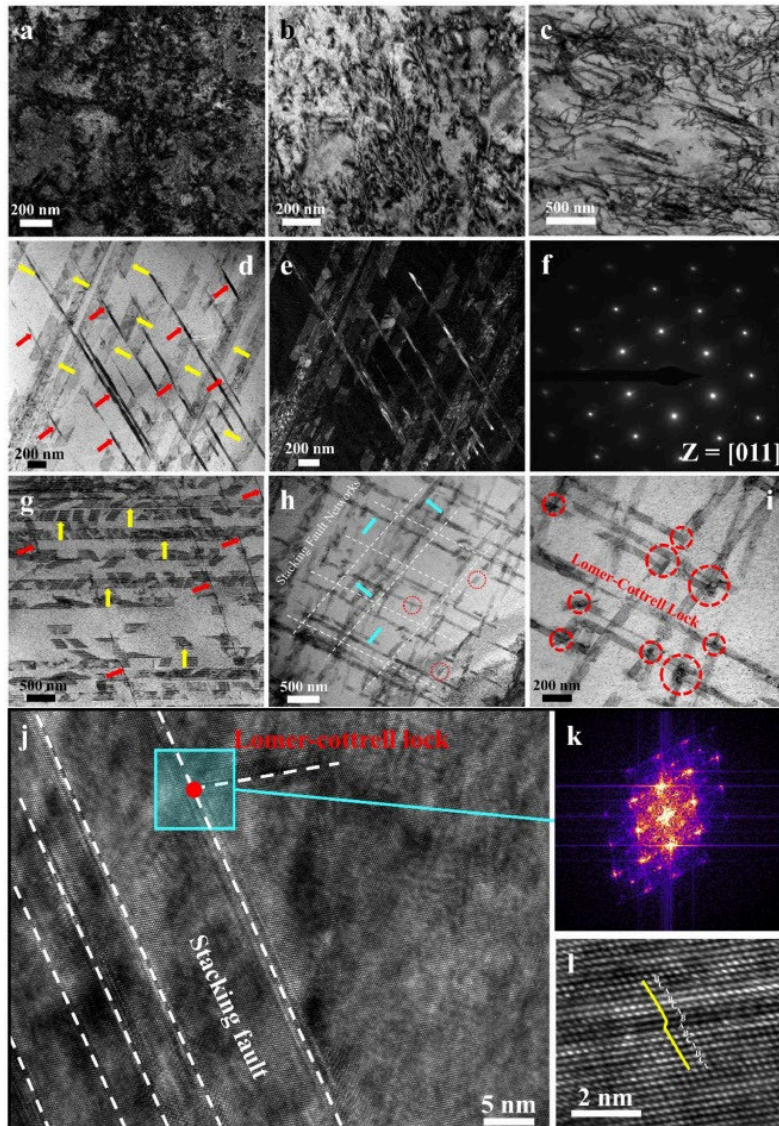
Fig. 6. Microstructure changes of SS and AG after stress loading. (a-b) BF images of SS and AG samples before the tensile tests, respectively. (c-d) BF images of SS and AG samples after the tensile tests, showing dislocation and SF characteristics in SS and AG samples, respectively. (e-f) DP and DF of (d), respectively. (g) BF image of AG samples after the tensile test, showing the SFs under different observation angles. (h) BF image of AG samples after the tensile test presenting the intersecting SFs on the {111} slip system. (i) BF image from (h) showing that LC locks are formed at the intersection of SF networks. (j) HRTEM image from (i) indicating the intersecting SF networks (white dotted line) and LC locks (red dot). (k) FFT image from (j), showing the existence of the intersecting SF. (l) An enlarged view of a representative SF from (j), demonstrating the BCABABCA-stacking sequence.

4. Discussion

4.1. Effects of compositions on the crystal structures of nano-precipitates

The obtained Ni_3Nb-type nano-precipitate in this HEA possesses an $L1_2$ structure rather than a $D0_{22}$ structure (common in Ni-based superalloys added with Nb (He et al., 2019; Yu et al., 2022; Zhao et al., 2022)). Therefore, it is worth exploring that why the Ni_3Nb phase in this HEA possesses a novel $L1_2$ structure. Here, Ni_3Nb-$L1_2$ and $D0_{22}$ structures are established. The formation energy per atom of Ni_3Nb-$L1_2$ and $D0_{22}$ models is described as follows:(3)$E_f=(E_{tot}-48\mu_{Ni}-16\mu_{Nb})/64$

As shown in **Fig. 5** (Models 4 and 5), the $D0_{22}$-Ni_3Nb model without Co/Fe/V substituting for Ni and Nb possesses a lower formation energy, indicating that the Ni_3Nb is easier to form in the $D0_{22}$ structure. However, when Co/Fe/V substitute for A and B sites by forming $(Ni_{24}Co_{18}Fe_6)(Nb_{10}V_4Fe_2)$, the energy is reverse, and the $L1_2$ structure is more stable in this composition.

To further investigate the effect of composition on the transformation from the $D0_{22}$ to $L1_2$ phase, the compositions of $Ni_{48}(Nb_{10}V_4Fe_2)$ and $Ni_{24}Co_{18}Fe_6(Nb_{16})$ for both $L1_2$ and $D0_{22}$ phases were established to see the influence of the A or B site substitution on the formation energy. When the Nb sites are partly substituted by V and Fe $[Ni_{48}(Nb_{10}V_4Fe_2)]$, the $D0_{22}$ structure still possesses a lower energy (**Fig. 7**a). However, when Ni sites are partly replaced by Co and Fe, the formation energy begins to reverse with the $L1_2$ structure possessing a lower energy (**Fig. 7**a). This feature indicates that the Ni-site substitution plays a main role, leading to the transformation from the $D0_{22}$ to $L1_2$ phase. In order to further verify the effect of Co or Fe substitution on the energy reversal, two structures without Fe $[Ni_{30}Co_{18}(Nb_{10}V_4Fe_2)]$ or Co $[Ni_{42}Fe_6(Nb_{10}V_4Fe_2)]$

at A site for both L1$_2$ and D0$_{22}$ phases were set up. The formation energy of Ni$_{30}$Co$_{18}$Nb$_{10}$V$_4$Fe$_2$ for L1$_2$ is lower than that of D0$_{22}$, while [Ni$_{42}$Fe$_6$(Nb$_{10}$V$_4$Fe$_2$)] for L1$_2$ is still higher than that of D0$_{22}$, as shown in **Fig. 7**a, indicating that the Co substituting for the Ni site can result in the structure transformation. Then, the effects of the Co content on the formation energy are further calculated, and compared for L1$_2$ and D0$_{22}$ phases, as presented in **Fig. 7**b. It is found that when 4Co substitutes for Ni sites, the formation energy of L1$_2$-Ni$_3$Nb begins to be lower than that of D0$_{22}$-Ni$_3$Nb. With a further increase in the Co content, the formation energies for both L1$_2$ and D0$_{22}$ structures decrease, tending to be more stable, especially for L1$_2$-Ni$_3$Nb. Finally, we further calculate the formation energy with only 4Co substituting for Ni sites [Ni$_{44}$Co$_4$(Nb$_{16}$)], and it is found that the D0$_{22}$ structure possesses a lower formation energy (L1$_2$: - 1.649 eV; D0$_{22}$: - 1.766 eV), i.e., only the 4Co substitution cannot induce the transformation from the D0$_{22}$ to L1$_2$ structure. The structure transformation is mainly determined by the Co substitution, but also depends on other elements doping in the Ni$_3$Nb-type nano-precipitates. The above results confirm that L1$_2$-Ni$_3$Nb nano-precipitates can exist stably in the composition of (Ni$_{24}$Co$_{18}$Fe$_6$)(Nb$_{10}$V$_4$Fe$_2$).
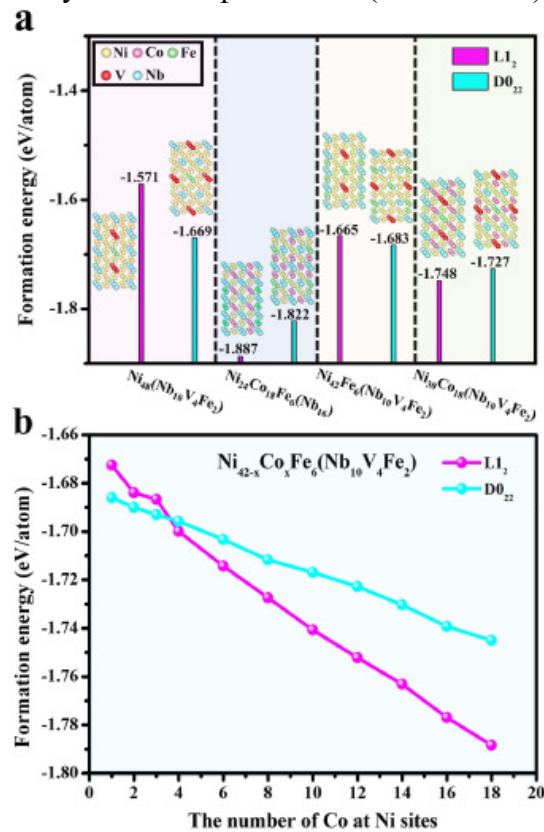

Fig. 7. Composition effects on the crystal structures of nano-precipitates. (a) Comparison of formation energies of L1$_2$-Ni$_3$Nb and D0$_{22}$-Ni$_3$Nb structures with various atom substituting for the A or B site. (b) Effect of the Co content on the formation energies of L1$_2$-Ni$_3$Nb and D0$_{22}$-Ni$_3$Nb.

4.2. Strengthening mechanisms

In this study, SS and AG were considered to possess the same grain size (**Fig. 2**) and dislocation density due to the same processing technology (the dislocation densities in SS and AG were estimated to be 3.04×10^{13} m^{-2} and 5.45×10^{13} m^{-2} from XRD, respectively). Hence, the contribution of the intrinsic strength, solid-solution hardening, grain-boundary hardening, and dislocation strengthening to SS and AG is considered to be the same. The yield-strength increment of AG can be completely attributed to precipitation strengthening ($\Delta\sigma_P$) and expressed as:(4)$\Delta\sigma_{0.2}=\Delta\sigma_p$

The precipitates can strengthen the alloy by a dislocation-bypassing mechanism (Orowan type) or particle-shearing mechanism, depending on the interaction between the moving dislocation and the precipitates (Wang et al., 2020). For the sake of evaluating the strengthening mechanism of precipitates, we discussed the bypassing mechanism at first. Generally, the Orowan mechanism occurs when the particles are large or incoherent with the matrix (Xiong et al., 2021). The increase of yield strength caused by the Orowan mechanism can be predicted by the following formula (He et al., 2019):(5)$\Delta\sigma_{orowan}=0.538Gbf^{1/2}r\ln(\frac{r}{2b})$ where $G = 60$ GPa (Jin et al., 2017) is the shear modulus, $b = 2a/2$ is the Burgers vector, r and f are the average particle diameter and the volume fraction (18% from APT result) of the precipitates, respectively. It can be seen from the calculation results that such a large strength increment (1,594 MPa) is obviously inconsistent with the experimental results. Hence, the precipitation enhancement mechanism in this HEA cannot be dominated by the Orowan mechanism.

When the particles are coherent with small sizes, the shearing mechanism plays a leading role (Xiong et al., 2021). According to the characteristics of precipitates (small sizes and coherent interfaces with the matrix) shown in **Fig. 3**, the particle-shearing mechanism should be the source of precipitation strengthening. Three major factors need to be considered when calculating the shear effect of particles by dislocations, including the coherency-strengthening ($\Delta\sigma_{CS}$) mechanism, modulus-strengthening ($\Delta\sigma_{MS}$) mechanism, and order strengthening ($\Delta\sigma_{OS}$) mechanism. It should be emphasized that these strengthening processes are carried out successively. The first two ($\Delta\sigma_{CS}$ and $\Delta\sigma_{MS}$) occur before dislocations shear precipitates, while the latter ($\Delta\sigma_{OS}$) takes place during shearing. In this case, the larger one of ($\Delta\sigma_{CS} + \Delta\sigma_{MS}$) or $\Delta\sigma_{OS}$ contributes to the total strength increment of the shear mechanism. The following formula can be used to calculate these strength increments (He et al.,

2016):

$$(6)\ \Delta\sigma_{CS}=M\cdot\alpha_\varepsilon(G\cdot\varepsilon)3/2(rf0.5Gb)1/2$$

$$(7)\ \Delta\sigma_{MS}=M\cdot0.0055(\Delta G)3/2(2fG)1/2(rb)(3m/2)-1$$

$$(8)\ \Delta\sigma_{OS}=M\cdot0.81\gamma APB2b(3\pi f8)1/2$$

Here we employ the parameters of $L1_2$-Ni_3Al, because **Eqs. (6-7)** are based on the $L1_2$ structure, and independent on the composition. $M = 3.06$ is the Taylor factor for an FCC polycrystalline matrix (He et al., 2016), $\alpha_\varepsilon = 2.6$ for the FCC structure (He et al., 2016), $\varepsilon = 0.2\%$ is the constrained lattice-parameter mismatch between the nanoscale precipitates and matrix measured from high-resolution TEM (HRTEM) images, $m = 0.85$ (He et al., 2016), ΔG is the shear-modulus mismatch between the matrix and the precipitates ($G = 77$ GPa in Ni_3Al), and $\gamma_{APB} = 0.12$ J/m^2 is the anti-phase boundary energy of the $L1_2$-Ni_3Al precipitates (He et al., 2016). The calculated results show that the yield strength can be increased by 322 MPa theoretically [$\Delta\sigma_{CS}$ (114 MPa) + $\Delta\sigma_{MS}$ (208 MPa) = 322 MPa; $\Delta\sigma_{OS}$ = 273 MPa]. But this feature is quite different from the experimental value (521 MPa), indicating that the parameters of $L1_2$-Ni_3Al are not suitable for $L1_2$-Ni_3Nb while calculating the strength contribution, which leads to the deviation of the calculated values. From **Eqs. (6-7)**, it is considered that the cause of deviation is closely related to ΔG and γ_{APB}. Because ΔG and γ_{APB} affect $\Delta\sigma_{MS}$ and $\Delta\sigma_{OS}$, respectively, and the relationship between $\Delta\sigma_{MS}$ and $\Delta\sigma_{OS}$ is the competition rather than superposition. Then we discuss ΔG and γ_{APB} separately.

First, we discuss the effect of ΔG. The experimental value of the strength increment is 521 MPa minus $\Delta\sigma_{CS}$. It can be calculated that ΔG should be 27 GPa; that is to say, the shear modulus of the $L1_2$-Ni_3Nb precipitate should be as high as 87 GPa. It is reported that the shear-modulus difference between the matrix phase and the precipitate with an FCC structure is usually small (He et al., 2019; Zhang et al., 2020; Ming et al., 2017). In addition, the shear-modulus difference between BCC and FCC phases with different structures is only 15 GPa (Liang et al., 2018). Therefore, the reason for the difference between strength calculations and experimental results should be independent of ΔG.

Then, γ_{APB} can be estimated to be $0.21 \sim 0.23$ J/m^2, considering the volume fraction of $18 \sim 22\%$. According to APT and first-principles calculations, the substitution of alloy elements into $L1_2$-Ni_3Nb results in the complex chemical composition of the precipitates. Studies have shown that the addition of other alloying elements in Ni_3Al has a great influence on the value of γ_{APB} (Li et al., 2022). Compared with Ni_3Al with the same $L1_2$ structure, a large number of Nb and V elements substituting the B site into $L1_2$-Ni_3Nb have a positive effect on the increase of γ_{APB} (Aykol et al., 2010), leading to a higher γ_{APB}.

By comparing the strengthening effects of $L1_2$-Ni_3(Al, Ti) and $L1_2$-Ni_3Nb with the same size and volume fraction, it is not difficult to see that the strengthening effect of $L1_2$-Ni_3Nb is more significant. Its advantages can be attributed to two reasons: (1) $L1_2$-Ni_3Nb possesses a higher antiphase domain boundary energy, which leads to greater ordered strengthening; (2) the lattice mismatch between the $L1_2$-Ni_3Nb and FCC matrix is very small, so the plasticity loss is very low while strengthening the alloy. Therefore, compared with the traditional $L1_2$-Ni_3Al-type-strengthened HEAs (under similar processing conditions), $L1_2$-Ni_3Nb-strengthened HEAs have better strength and plasticity (He et al., 2019, 2016; Zhang et al., 2019; Peng et al., 2019), as shown in **Fig. 8**a. The newly-developed HEA exhibits an excellent strength-ductility product (as high as 65 GPa%), which is much higher than those of other high-performance materials (about 10 - 45 GPa%) (Hou et al., 2021; He et al., 2017a; Kim et al., 2015), as shown in **Fig. 8**b.
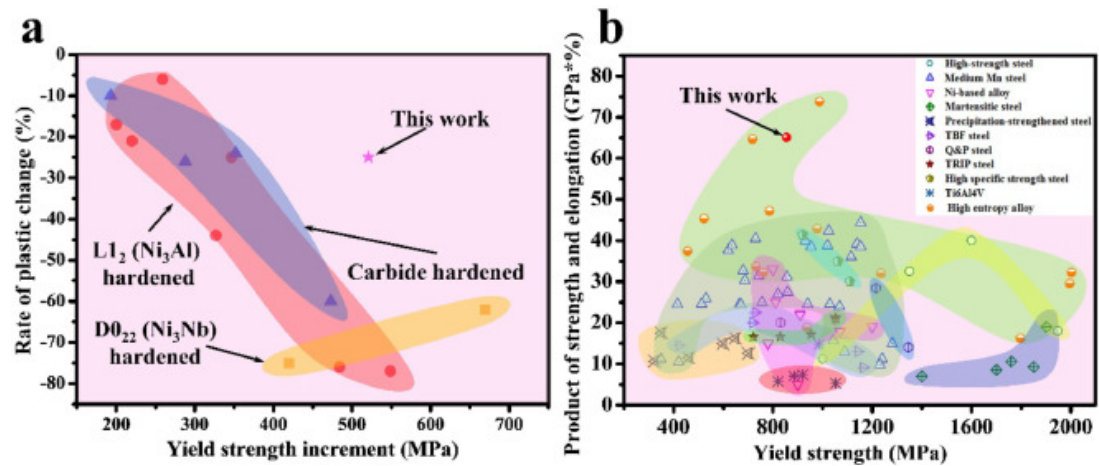

Fig. 8. Ashby plot showing the advantages of the new HEA and the strategy to design HEAs with both excellent strength and ductility. (a) Comparative results of $L1_2$-Ni_3Nb with $L1_2$-Ni_3Al, $D0_{22}$-Ni_3Nb, and carbides on the increase in the yield strength and plastic-change rate ($\delta AG-\delta SS\delta SS$, where δ is plastic) of the alloys. (b) Yield strength and strength-ductility product of the AG sample and other high-performance materials.

In addition, this new $L1_2$-Ni_3Nb-strengthened HEAs may also possess satisfactory mechanical properties at high temperature. Generally, compared with conventional superalloys, single-phase HEAs can show better mechanical properties at high temperature due to the stronger lattice distortion effect (Kim et al., 2021). A unique microstructure composed of ordered nano-precipitates embedded in a disordered matrix can be observed in common Co- (Sato et al., 2006), Ni- (Reed, 2008), FeNi- (Zhang et al., 2018) based superalloys. For example, some commercial Ni-based

superalloys (Erickson, 1996) possess excellent high-temperature mechanical properties derived from the precipitation strengthening provided by a large number of coherent γ' (Ni₃Al) nano-precipitates and solid solution strengthening. The small lattice mismatch between the martix and γ' phase can ensure the high temperature thermal stability of the alloys by reducing the coarsening rate of precipitates (Kim et al., 2021), and thus plays a key role in high-temperature performance (Long et al., 2016). For AG-HEA, the close-packed FCC lattice structure of the matrix can delay the transmission of atoms (He et al., 2017b). The new $L1_2$-Ni₃Nb nano-precipitates embedded in the matrix reduces the diffusion rate between the two phases due to the small lattice mismatch (0.2%), which can not only reduce the coarsening rate of the precipitates (Kim et al., 2021), but also delay the relaxation of the interface strain field, thereby inhibiting high temperature softening and improving creep resistance (Henderson, 1988).

4.3. Enhancements of plasticity and work hardening

The appearance of a large number of SFs in AG indicates that the SFE of the matrix is lower than that of SS. Comparing the microstructures of AG and SS, it can be attributed to the contribution of nano-precipitates (Xu et al., 2021). After aging, a large number of high SFE-forming elements (including Ni and Nb atoms) are separated out from the matrix to form precipitates, resulting in the decrease of the SFE of the matrix (Fan et al., 2020). Thus, a/2 〈110〉 unit dislocation can dissociate into a pair of a/6 〈112〉 Shockley partial dislocations with a SF band between them (Fan et al., 2020). From the morphology of the SFs shown in **Fig. 6**h, both narrow and wide SF bands (marked with red circle and blue arrow, respectively) can be observed, indicating that the extended dislocations continuously form during deformation of AG samples. Compared with one-dimensional defects, SFs caused by wrong stacking between atomic planes can provide larger plasticity (Swygenhoven et al., 2004; Shih et al., 2021). The lower the SFE is, the wider the equilibrium width of the SF area is. Unless the slip of partial dislocations is hindered, the width of SFs band will tend to expand the equilibrium width of extended dislocations (Goyal et al., 2021; Jung et al., 2017), contributing to the excellent plasticity. Similar to the TWIP effect (Gutierrez et al., 2011), the dynamic formation and refinement of these SF networks can prevent dislocations movement by reducing the mean free path. In addition, it also helps increase the work hardening response (Yang et al., 2019).

When the extended dislocations on the two intersecting {111} planes meet, the first contacting partial dislocations interact and then another partial dislocation on the non-

sliding {100} plane is formed, that is, the sessile stair-rod dislocation (Lomer-Cottrell lock), as presented in **Fig. 6**i. This partial dislocation is a group of immobile dislocation structure, because it involves a SF band on the two intersecting slip planes. Thus it can neither slide on the two intersecting slip planes nor on its own slip plane, resulting in the failure of this dislocation to slide (Wu et al., 2009). The inherent high structural stability of the partial dislocation can resist the dissociation and become the blockage of subsequent dislocations (Chen et al., 2020). On the other hand, because the partial dislocation is located at the intersection of SF network, the dislocation segment is pinned, which makes the SF network more stable (Wu et al., 2009). Therefore, the blocking effect of LC locks on dislocations plays an important role in the stable and progressive work-hardening of AG-HEA, as shown in **Fig. 1**. Whether it is SF network or LC lock, the dynamic formation increases the hardening modulus to match the increase in strength so that the strain hardening exponent increases (Gao et al., 2020). By increasing the work hardening rate to delay the occurrence of necking, the strength-ductility of AG-HEA is improved synergistically.

The large plasticity of AG-HEA is also closely related to the following two reasons: On one hand, from the point of view of precipitates, the complete coherent relationship between the FCC matrix and $L1_2$ nano-precipitate and its ultrafine size will not seriously affect the plasticity of the HEA. A lower lattice-mismatch ratio can reduce the nucleation barrier of the precipitates, and will not lead to uneven coarsening, so that the external force can be evenly dispersed on the interface between the precipitates and matrix (Du et al., 2020). As a result, the stress concentration is alleviated, effectively inhibiting the nucleation of cracks (Jiang et al., 2017; Utt et al., 2020). Moreover, the incorporation of Co and Fe in the $L1_2$ phase can also improve the inherent ductility (Yang et al., 2018). In a word, a large number of SF networks and LC are continuously generated in the deformation process, resulting in the AG-HEA still possessing large plasticity and excellent work-hardening ability.

 Conclusion

A novel non-equiatomic $Ni_{35}(CoFe)_{55}V_5Nb_5$ HEA is developed successfully, possessing an excellent strength and ductility synergy. The yield and tensile strengths at room temperature are 855 MPa and 1,300 MPa, respectively, along with an excellent ductility of ~ 50%. A completely-new type of bifunctional $L1_2$-Ni_3Nb type precipitates $(Ni_{24}Co_{18}Fe_6)_3(Nb_{10}V_4Fe_2)$ with a tiny size of ~ 5 nm in diameter is introduced. When some Ni atoms are substituted by Co and Fe while Nb by V and Fe in Ni_3Nb-type precipitates, the formation energy of $(Ni_{24}Co_{18}Fe_6)_3(Nb_{10}V_4Fe_2)$ with a $L1_2$ structure is

lower than D0$_{22}$-Ni$_3$Nb, forming the Ni$_3$Nb-type precipitates with a L1$_2$ structure. The novel precipitates provide two-fold functions. On the one hand, L1$_2$-(Ni$_{24}$Co$_{18}$Fe$_6$)$_3$(Nb$_{10}$V$_4$Fe$_2$) nano-precipitates have a high anti-phase boundary energy, contributing to a significant increment in yield strength ($\sim$ 520 MPa) through precipitation strengthening. Moreover, the precipitates lower the SFE of the alloy matrix, changing the main deformation mode from dislocation slip to SFs-dominated deformation. The continuous formation of SF networks during deformation contributes to the large ductility while LC locks during deformation to work hardening. The design of this bifunctional nano-precipitates and the regulation of the SFE through solute precipitation in the HEA matrix can be applied in many other alloy systems.

Author statement

Yang Zhang and Zhongwu Zhang designed the study. Liyuan Liu, Junpeng Li, Mingyu Fan, Xiyu Wang and Guangchuan Wu carried out the main experiments. Liyuan Liu, Yang Zhang, Zengbao Jiao, Chain Tsuan Liu, Peter K Liaw and Zhongwu Zhang analyzed the data and wrote the main draft of the paper. Zhongbo Yang and Junhua Luan conducted the characterizations. All authors contributed to the discussion of the results and commented on the manuscript.

Data availability

The data that support the findings of this study is available from the corresponding authors upon reasonable request.

Declaration of Competing Interest

The authors declare no conflict of interest.

Acknowledgments

References

Abdolrahim, N., Mastorakos, I.N., Zbib, H.M., 2012. Precipitate strengthening in nanostructured metallic material composites. Phil. Mag. Lett. 92, 597–607.

Aykol, M., Mekhrabov, A.O., Akdeniz, M.V., 2010. Effect of vanadium on atomic ordering characteristics and anti-phase boundary energies of B2-FeCo alloys.

Intermetallics 18, 893–899.

Bahramyan, M., Mousavian, R.T., Brabazon, D., 2020. Study of the plastic deformation mechanism of TRIP-TWIP high entropy alloys at the atomic level. Int. J.

Plasticity 127, 102649.

Baig, Muneer., Seikh, A.H., Rehman, A.U., Mohammed, J.A., Hashmi, F.H., Ragab, S.M., 2021. Microstructure evaluation study of Al5083 alloy using EBSD technique after processing with different ECAP processes and temperatures. Crystals 11, 862–874.

Cantor, B., Chang, I.T.H., Knight, P., Vincent, A.J.B., 2004. Microstructural development in equiatomic multicomponent alloys. Mat. Sci. Eng. A 375–377, 213–218.

Chen, S., Oh, H.S., Gludovatz, B., Kim, S.J., Park, E.S., Zhang, Z., Ritchie, R.O., Yu, Q., 2020. Real-time observations of TRIP-induced ultrahigh strain hardening in a dual-phase CrMnFeCoNi high-entropy alloy. Nat. Commun. 11, 826.

Ding, Q., Zhang, Y., Chen, X., Fu, X., Chen, D., Chen, S., Gu, L., Wei, F., Bei, H., Gao, Y., Wen, M., Li, J., Zhang, Z., Zhu, T., Ritchie, R.O., Yu, Q., 2019. Tuning element distribution, structure and properties by composition in high-entropy alloys. Nature 574, 223–227.

Ding, Z.Y., He, Q.F., Wang, Q., Yang, Y., 2018. Superb strength and high plasticity in Laves phase rich eutectic medium-entropy-alloy nanocomposites. Int. J. Plasticity

106, 57–72.

Du, X.H., Li, W.P., Chang, H.T., Yang, T., Duan, G.S., Wu, B.L., Huang, C., Chen, F.R., Liu, C.T., Chuang, W.S., Lu, Y., Sui, M.L., Huang, E.W., 2020. Dual heterogeneous structures lead to ultrahigh strength and uniform ductility in a Co-Cr-Ni medium-entropy alloy. Nat. Commun. 11, 2390.

Erickson, G., 1996. The development and application of CMSX-10. Superalloys 1996, 35–44.

Fan, L., Yang, T., Zhao, Y., Luan, J., Zhou, G., Wang, H., Jiao, Z., Liu, C.T., 2020. Ultrahigh strength and ductility in newly developed materials with coherent

nanolamellar architectures. Nat. Commun. 11, 6240.

Farkoosh, A.R., Dunand, D.C., Seidman, D.N., 2020. Tungsten solubility in L12-ordered Al3Er and Al3Zr nanoprecipitates formed by aging in an aluminum matrix.

J. Alloy. Compd. 820, 153383.

Feng, R., Feng, B., Gao, M.C., Zhang, C., Neuefeind, J.C., Poplawsky, J.D., Ren, Y., An,

K., Widom, M., Liaw, P.K., 2021. Superior high-temperature strength in a supersaturated refractory high-entropy alloy. Adv. Mater. 33, 2102401.

Feng, X.B., Zhang, J.Y., Wang, Y.Q., Hou, Z.Q., Wu, K., Liu, G., Sun, J., 2017a. Size effects on the mechanical properties of nanocrystalline NbMoTaW refractory high entropy alloy thin films. Int. J. Plasticity 95, 264–277.

Feng, X.B., Fu, W., Zhang, J.Y., Zhao, J.T., Li, J., Wu, K., Liu, G., Sun, J., 2017b. Effects of nanotwins on the mechanical properties of AlxCoCrFeNi high entropy alloy thin films. Scr. Mater. 139, 71–76.

Fu, W.J., Gan, K.F., Huang, Y.J., Ning, Z.L., Sun, J.F., Cao, F.Y., 2021. Elucidating the transition of cryogenic deformation mechanism of CrMnFeCoNi high entropy alloy. J. Alloy. Compd. 872, 159606.

Gao, Y.F., Zhang, W., Shi, P.J., Ren, W.L., Zhong, Y.B., 2020. A mechanistic interpretation of the strength-ductility trade-off and synergy in lamellar microstructures.

Mater. Today Adv. 8, 100103.

George, E.P., Raabe, D., Ritchie, R.O., 2019. High-entropy alloys. Nat. Rev. Mater. 4, 515–534.

Goyal, A., Li, Y., Chernatynskiy, A., Jayashankar, J.S., Kautzky, M.C., Sinnott, S.B., Phillpot, S.R., 2021. The influence of alloying on the stacking fault energy of gold from density functional theory calculations. Comput. Mater. Sci. 188, 110236.

Gutierrez-Urrutia, I., Raabe, D., 2011. Dislocation and twin substructure evolution during strain hardening of an Fe–22wt.% Mn–0.6wt.% C TWIP steel observed by electron channeling contrast imaging. Acta Mater. 59, 6449–6462.

Han, B., Wei, J., Tong, Y., Chen, D., Zhao, Y., Wang, J., He, F., Yang, T., Zhao, C., Shimizu, Y., Inoue, K., Nagai, Y., Hu, A., Liu, C.T., Kai, J.J., 2018. Composition evolution of gamma prime nanoparticles in the Ti-doped CoFeCrNi high entropy alloy. Scr. Mater. 148, 42–46.

Hao, J., Wu, G.H., Liu, W.C., Sun, J.W., Ding, W.J., 2021. Role of extrusion temperature on the microstructure evolution and tensile properties of an ultralight Mg-Li-Zn-Er alloy. J. Alloy. Compd. 876, 160181.

Hasan, M.N., Liu, Y.F., An, X.H., Gu, J., Song, M., Cao, Y., Li, Y.S., Zhu, Y.T., Liao, X.Z., 2019. Simultaneously enhancing strength and ductility of a high-entropy alloy via gradient hierarchical microstructures. Int. J. Plasticity 123, 178–195.

He, B.B., Hu, B., Yen, H.W., Cheng, G.J., Wang, Z.K., Luo, H.W., Huang, M.X., 2017a. High dislocation density–induced large ductility in deformed and partitioned steels. Science 357, 1029–1032.

He, F., Chen, D., Han, B., Wu, Q., Wang, Z., Wei, S., Wei, D., Wang, J., Liu, C.T., Kai, J.J., 2019. Design of D022 superlattice with superior strengthening effect in high entropy alloys. Acta Mater. 167, 275–286.

He, J.Y., Wang, H., Huang, H.L., Xu, X.D., Chen, M.W., Wu, Y., Liu, X.J., Nieh, T.G., An, K., Lu, Z.P., 2016. A precipitation-hardened high-entropy alloy with outstanding tensile properties. Acta Mater. 102, 187–196.

He, J.Y., Wang, H., Wu, Y., Liu, X.J., Nieh, T.G., Lu, Z.P., 2017b. High-temperature plastic flow of a precipitation-hardened FeCoNiCr high entropy alloy. Mat. Sci. Eng. A 686, 34–40.

Henderson, P., 1988. Dislocations at γ/γ' interfaces during the creep of nickel-base superalloys. Scr. Metall. 22, 1103–1107.

Hou, P., Li, Y., Chae, D., Ren, Y., An, K., Choo, H., 2021. Lean duplex TRIP steel: role of ferrite in the texture development, plastic anisotropy, martensitic transformation kinetics, and stress partitioning. Materialia 15, 100952.

Jiang, S., Wang, H., Wu, Y., Liu, X., Chen, H., Yao, M., Gault, B., Ponge, D., Raabe, D., Hirata, A., Chen, M., Wang, Y., Lu, Z., 2017. Ultrastrong steel via minimal lattice misfit and high-density nanoprecipitation. Nature 544, 460–464.

Jiao, Z.B., Luan, J.H., Miller, M.K., Yu, C.Y., Liu, C.T., 2015. Effects of Mn partitioning on nanoscale precipitation and mechanical properties of ferritic steels strengthened by NiAl nanoparticles. Acta. Mater. 84, 283–291.

Jin, K., Gao, Y.F., Bei, H., 2017. Intrinsic properties and strengthening mechanism of monocrystalline Ni-containing ternary concentrated solid solutions. Mat. Sci.
Eng. A 695, 74–79.

Jung, J., Yoon, J.I., Kim, J.G., Latypov, M.I., Kim, J.Y., Kim, H.S., 2017. Continuum understanding of twin formation near grain boundaries of FCC metals with low stacking fault energy. NPJ Comput. Mater. 3, 21.

Kaushik, L., Kim, M.S., Singh, J., Kang, J.H., Heo, Y.U., Suh, J.Y., Choi, S.H., 2021. Deformation mechanisms and texture evolution in high entropy alloy during cold rolling. Int. J. Plasticity 141, 102989.

Khater, H.A., Monnet, G., Terentyev, D., Serra, A., 2014. Dislocation glide in Fe–carbon solid solution: from atomistic to continuum level description. Int. J. Plasticity 62, 34–49.

Kim, S.H., Kim, H., Kim, N.J., 2015. Brittle intermetallic compound makes ultrastrong low-density steel with large ductility. Nature 518, 77–79.

Kim, W.C., Na, M.Y., Kwon, H.J., Na, Y.S., Won, J.W., Chang, H.J., Lim, K.R., 2021. Designing L21-strengthened Al-Cr-Fe-Ni-Ti complex concentrated alloys for high temperature applications. Acta Mater. 211, 116890.

Kivy, M.B., Zaeem, M.A., 2017. Generalized stacking fault energies, ductilities, and twinnabilities of CoCrFeNi-based face-centered cubic high entropy alloys. Scr.
Mater. 139, 83–86.

Koizumi, K., Suzuki, S., Yamanaka, K., Lee, B.S., Sato, K., Li, Y., Kurosu, S., Matsumoto, H., Chiba, A., 2013. Strain-induced martensitic transformation near twin boundaries in a biomedical Co-Cr-Mo alloy with negative stacking fault energy. Acta Mater. 61, 1648–1661.

Li, W.D., Xie, D., Li, D.Y., Zhang, Y., Gao, Y.F., Liaw, P.K., 2021. Mechanical behavior of high-entropy alloys. Prog. Mater. Sci. 118, 100777.

Li, Y.L., Qiang, W.J., 2022. Ordered structure and solute-suppressed atomic ordering in iron-cobalt alloys. Comp. Mater. Sci. 202, 111005.

Li, Z., Zhao, S., Ritchie, R.O., Meyers, M.A., 2019. Mechanical properties of high-entropy alloys with emphasis on face-centered cubic alloys. Prog. Mater. Sci. 102, 296–345.

Li, Z.M., Pradeep, K.G., Deng, Y., Raabe, D., Tasan, C.C., 2016. Metastable high-entropy dual-phase alloys overcome the strength–ductility trade-off. Nature 534,
227–230.

Liang, Y.J., Wang, L., Wen, Y., Cheng, B., Wu, Q., Cao, T., Xiao, Q., Xue, Y., Sha, G., Wang, T., Ren, Y., Li, X., Wang, L., Wang, F., Cai, H., 2018. High-content ductile coherent nanoprecipitates achieve ultrastrong high-entropy alloys. Nat. Commun. 9, 4063.

Liu, L.Y., Zhang, Y., Han, J.H., Wang, X.Y., Jiang, W.Q., Liu, C.T., Zhang, Z.W., Liaw, P.K., 2021. Nanoprecipitate-strengthened high-entropy alloys. Adv. Sci. https:// doi.org/10.1002/advs.202100870.

Long, H., Wei, H., Liu, Y., Mao, S., Zhang, J., Xiang, S., Chen, Y., Gui, W., Li, Q., Zhang, Z., 2016. Effect of lattice misfit on the evolution of the dislocation structure in Ni-based single crystal superalloys during thermal exposure. Acta Mater. 120, 95–107.

Maity, T., Prashanth, K.G., Balci, O., Kim, J.T., Schoberl, T., Wang, Z., Eckert, J., 2018. Influence of severe straining and strain rate on the evolution of dislocation structures during micro-/nanoindentation in high entropy lamellar eutectics. Int. J. Plasticity 113, 255–268.

Ming, K.S., Bi, X.F., Wang, J., 2017. Realizing strength-ductility combination of coarse-grained Al0.2Co1.5CrFeNi1.5Ti0.3 alloy via nano-sized, coherent precipitates. Int. J. Plasticity 109, 121–136.

Otto, F., Dlouhy, A., Somsen, Ch., Bei, H., Eggeler, G., George, E.P., 2013. The influences of temperature and microstructure on the tensile properties of a CoCrFeMnNi high-entropy alloy. Acta Mater. 61, 5743–5755.

Pan, Q., Zhang, L., Fneg, R., Lu, Q., An, K., Chuang, A.C., Poplawsky, J.D., Liaw, P.K., Lu, L., 2021. Gradient-cell-structured high-entropy alloy with exceptional strength and ductility. Science 374, 984–989.

Pandey, A., Kabirian, F., Hwang, J.H., Choi, S.H., Khan, A.S., 2015. Mechanical responses and deformation mechanisms of an AZ31 Mg alloy sheet under dynamic and simple shear deformations. Int. J. Plasticity 68, 111–131.

Peng, J., Li, Z., Fu, L., Ji, X., Pang, Z., Shan, A., 2019. Carbide precipitation strengthening in fine-grained carbon-doped FeCoCrNiMn high entropy alloy. J. Alloy. Compd. 803, 491–498.

Philippe, T., Voorhees, P.W., 2013. Ostwald ripening in multicomponent alloys. Acta Mater. 61, 4237–4244.

Reed, R.C., 2008. The Superalloys: Fundamentals and Applications. Cambridge university press.

Ritchie, R.O., 2011. The conflicts between strength and toughness. Nat. Mater. 10, 817–822.

Sato, J., Omori, T., Oikawa, T., Ohnuma, I., Kainuma, R., Ishida, K., 2006. Cobalt-base high-temperature alloys. Science 312, 5770.

Scott, K., Saal, J.E., Meredig, B., Thompson, A., Doak, J.M., Aykol, M., Ruhl, S., Wolverton, C., 2015. The open quantum materials database (OQMD): assessing the accuracy of DFT formation energies. NPJ. Comput. Mater. 1, 15010.

Shi, P.J., Ren, W.L., Zhang, T.X., Ren, Z.M., Hou, X.L., Peng, J.C., Hu, P.F., Gao, Y.F., Zhong, Y.B., Liaw, P.K., 2019. Enhanced strength–ductility synergy in ultrafinegrained eutectic high-entropy alloys by inheriting microstructural lamellae. Nat. Commun. 10, 489.

Shih, M., Miao, J., Mills, M., Ghazisaeidi, M., 2021. Stacking fault energy in concentrated alloys. Nat. Commun. 12, 3590–3600.

Song, M., Zhou, R., Gu, J., Wang, Z., Ni, S., Liu, Y., 2020. Nitrogen induced heterogeneous structures overcome strength-ductility trade-off in an additively manufactured high-entropy alloy. Appl. Mater. Today 18, 100498.

Swygenhoven, H.V., Derlet, P.M., Froseth, A.G., 2004. Stacking fault energies and slip in nanocrystalline metals. Nat. Mater. 3, 399–403.

Tabachnikova, E.D., Podolskiy, A.V., Laktionova, M.O., Bereznaia, N.A., Tikhonovsky, M.A., Tortika, A.S., 2017. Mechanical properties of the CoCrFeNiMnVx high entropy alloys in temperature range 4.2-300K. J. Alloy. Compd. 698, 501–509.

Takeuchi, A., Inoue, A., 2005. Classification of bulk metallic glasses by atomic size difference, heat of mixing and period of constituent elements and its application to characterization of the main alloying element. Mater. Trans. 46, 2817–2829.

Utt, D., Lee, S., Stukowski, A., Oh, S.H., Dehm, G., Albe, K., 2020. Jerky motion of dislocations in high-entropy alloys: the linkage between local Peierls stress uctuations and dislocation mobility. https://arxiv.org/pdf/2007.11489.pdf.

Wang, C.Y., Cepeda-Jimenez, C.M., Perez-Prado, M.T., 2020. Dislocation-particle interactions in magnesium alloys. Acta Mater. 194, 190–206.

Wang, K.Y., Ning, Z.L., Li, M.W., Sun, J.F., Huang, Y.J., 2021. Shear punching of a Co20Cr20Fe20Ni20Mn15Cu5 high entropy alloy. J. Alloy. Compd. 887, 161415.

Wei, D., Li, X., Jiang, J., Heng, W., Koizumi, Y., Choi, M.W., Lee, B.J., Kim, H.S., Kato, H., Chiba, A., 2019. Novel Co-rich high performance twinning-induced plasticity (TWIP) and transformation-induced plasticity (TRIP) high-entropy alloys. Scr. Mater. 165, 39–43.

Wu, X.L., Zhu, Y.T., Wei, Y.G., Wei, Q., 2009. Strong strain hardening in nanocrystalline nickel. Phys. Rev. Lett. 103, 205504.

Wu, Y., Bonisch, M., Alkan, S., Abuzaid, W., Sehitoglu, H., 2018. Experimental determination of latent hardening coefficients in FeMnNiCoCr. Int. J. Plasticity 105, 239–260.

Xiong, Z.P., Timokhina, I., Pereloma, E., 2021. Clustering, nano-scale precipitation and strengthening of steels. Prog. Mater. Sci. 118, 100764.

Xu, S.S., Zhao, Y., Chen, D., Sun, L.W., Chen, L., Tong, X., Liu, C.T., Zhang, Z.W., 2019. Nanoscale precipitation and its influence on strengthening mechanisms in an ultra-high strength low-carbon steel. Int. J. Plasticity 113, 99–110.

Xu, W.W., Yin, G.H., Xiong, Z.Y., Yu, Q., Gang, T.Q., Chen, L.J., 2021. Plasticity-induced stacking fault behaviors of γ′ precipitates in novel CoNi-based superalloys. J. Mater. Sci. Technol. 90, 20–29.

Yang, T., Zhao, Y.L., Luan, J.H., Han, B., Wei, J., Kai, J.J., Liu, C.T., 2019. Nanoparticles-strengthened high-entropy alloys for cryogenic applications showing an exceptional strength-ductility synergy. Scr. Mater. 164, 30–35.

Yang, T., Zhao, Y.L., Tong, Y., Jiao, Z.B., Wei, J., Cai, J.X., Han, X.D., Chen, D., Hu, A., Kai, J.J., Lu, K., Liu, Y., Liu, C.T., 2018. Multicomponent intermetallic nanoparticles and superb mechanical behaviors of complex alloys. Science 362, 933–937.

Yeh, J.W., Chen, S.K., Lin, S.J., Gan, J.Y., Chen, T.S., Shen, T.T., Tsau, C.H., Chang, S.Y.,

2004. Nanostructured high-entropy alloys with multiple principal elements: novel alloy design concepts and outcomes. Adv. Eng. Mater. 6, 299–303.

Yuan, Y., Wu, Y., Tong, X., Zhang, H., Wang, H., Liu, X.J., Ma, L., Suo, H.L., Lu, Z.P., 2017. Rare-earth high-entropy alloys with giant magnetocaloric effect. Acta Mater. 125, 481–489.

Zhang, B., Yan, F., Zhao, M., Tao, N., Lu, K., 2018. Combined strengthening from nanotwins and nanoprecipitates in an iron-based superalloy. Acta Mater. 151, 310–320.

Zhang, D.D., Zhang, J.Y., Kuang, J., Liu, G., Sun, J., 2021. Superior strength-ductility synergy and strain hardenability of Al/Ta co-doped NiCoCr twinned medium entropy alloy for cryogenic applications. Acta Mater. 220, 117288.

Zhang, K., Wen, H.Y., Zhao, B.B., Dong, X.P., Zhang, L.T., 2019. Precipitation behavior and its impact on mechanical properties in an aged carbon-containing

Al0.3Cu0.5CrFeNi2 high-entropy alloy. Mater. Charact. 155, 109792.

Zhang, T.W., Ma, S.G., Zhao, D., Wu, Y.C., Zhang, Y., Wang, Z.H., Qiao, J.W., 2020. Simultaneous enhancement of strength and ductility in a NiCoCrFe high-entropy alloy upon dynamic tension: micromechanism and constitutive modeling. Int. J. Plasticity 124, 226–246.

Zhang, Y.H., Zhuang, Y., Hu, A., Kai, J.J., Liu, C.T., 2017. The origin of negative stacking fault energies and nano-twin formation in face-centered cubic high entropy alloys. Scr. Mater. 130, 96–99.

Zhao, Y.L., Li, Y.R., Yeli, G.M., Luan, J.H., Liu, S.F., Lin, W.T., Chen, D., Liu, X.J., Kai, J.J., Liu, C.T., Yang, T., 2022. Anomalous precipitate-size-dependent ductility in multicomponent high-entropy alloys with dense nanoscale precipitates. Acta Mater. 223, 117480.

Zhao, Y.X., 2020. Combined effect of nanoparticle and grain refinement on yield stress of nanocomposite. Philos. Mag. 100, 267–311.